

# Group Sparsity Methods for Compressive Space-Frequency Channel Estimation and Spatial Equalization in Fluid Antenna System

Xuehui Dong, *Student Member, IEEE*, Kai Wan, *Member, IEEE*, Shuangyang Li, *Member, IEEE*, Robert Caiming Qiu, *Fellow, IEEE*, and Giuseppe Caire, *Fellow, IEEE*

**Abstract**—Fluid Antenna System (FAS) unlocks unprecedented flexibility in wireless channel optimization through spatial reconfigurability. However, its practical deployment is hindered by the coupled challenges posed by high-dimensional channel estimation and real-time position optimization. This paper bridges wireless propagation physics with compressed sensing theory to address these challenges through three aspects. First, we establish a group-sparse recovery framework for space-frequency characteristics (SFC) in FAS, formally characterizing leakage-induced sparsity degradation from limited aperture and bandwidth as a structured group-sparsity problem. By deriving dictionary-adapted group restricted isometry property (D-GRIP), we prove tight recovery bounds for a convex  $\ell_1/\ell_2$ -mixed norm optimization formulation that preserves leakage-aware sparsity patterns. Second, we develop a Descending Correlation Group Orthogonal Matching Pursuit (DC-GOMP) algorithm that systematically relaxes leakage constraints to reduce subcoherence. This approach enables robust FSC recovery with accelerated convergence and superior performance compared to conventional compressive sensing methods like OMP or GOMP. Third, we formulate spatial equalization (SE) as a mixed-integer linear programming (MILP) problem, ensuring optimality through the branch-and-bound method. To achieve real-time implementability while maintaining near-optimal performance, we complement this with a greedy algorithm. Simulation results demonstrate the proposed channel estimation algorithm effectively resolves energy misallocation and enables recovery of weak details, achieving superior recovery accuracy and convergence rate. The SE framework suppresses deep fading phenomena and reduces hardware deployment overhead while maintaining equivalent link reliability.

**Index Terms**—Fluid antenna system, channel estimation, spatial equalization, compressed sensing, group sparsity.

## I. INTRODUCTION

The increasing demands of 6G wireless networks, such as terabit-per-second data rates, centimeter-level positioning accuracy, and ultra-reliable low-latency communications, are fundamentally reshaping antenna system design. Conventional massive MIMO architectures, while successful in past generations' deployments, face inherent limitations imposed by their fixed half-wavelength spacing configurations. According to the recent release by the IEEE Technical Committees [1], there are three critical bottlenecks that hinder the advancement of wireless communications: (i)

the spatial degrees of freedom (DoFs) ceiling caused by static array geometries, particularly detrimental in near-field and rich-scatter scenarios; (ii) the robustness dealing with the challenging scenarios, especially the severe fading and extremely low signal-to-noise ratio (SNR) environments; (iii) the dynamic channel tracking challenges in high-mobility or fast-varying environments where conventional beam alignment methods incur prohibitive overhead. To break these bottlenecks, new antenna structures need to be developed.

Fluid Antenna System (FAS), also known as Movable Antenna System in some references, presents a disruptive solution by transcending the rigid structure of legacy arrays. In general, FAS refers to any software-controllable fluidic, dielectric, or conductive structures, including but not limited to liquid-based antennas, pixel-based antennas, and metasurface-design antennas, that can dynamically reconfigure their shape, size, position, length, orientation, and other radiation characteristics. FAS enables active reshaping of spatial sampling patterns, effectively converting physical array reconfiguration into enhanced signal space dimensionality. This paradigm shift, as demonstrated in recent works [2], [3], allows real-time adaptation to multipath geometry for achieving high spatial diversity gain, high spectral efficiency, and robust massive connectivity [4]–[6].

Recent theoretical advancements have fundamentally redefined the information-theoretic limits of FAS, establishing a new paradigm for spatial resource optimization. The seminal work by Wong *et al.* [3] introduced the spatial microdiversity principle, rigorously proving through stochastic geometry that sub-wavelength FAS configurations surpass conventional multi-antenna maximum ratio combining (MRC) systems in terms of the diversity order. This theoretical framework was subsequently extended in [7], which established the existence of a strictly dominant diversity-multiplexing trade-off region for FAS compared to traditional MIMO architectures under asymptotic SNR conditions. The spatial sampling theorem developed by Xu *et al.* [8] generalized these results to multi-user environments, demonstrating FAS capacity scaling laws that asymptotically approach the theoretical upper bounds through adaptive spatial dimension manipulation. A pivotal advancement emerged in [6], where the hardware-performance decoupling theorem formally resolved the longstanding complexity-reliability trade-off, showing that single-radio-chain FAS achieves near-optimal reliability comparable to multi-chain MRC systems. The mathematical equivalence between FAS and ideal MRC systems in terms of Shannon capacity scaling is established in [9] under spatial continuum assumptions.

X. Dong, K. Wan, and R. C. Qiu are with the School of Electronic Information and Communications, Huazhong University of Science and Technology, 430074 Wuhan, China, (e-mail: {xuehuidong, kai\_wan, caiming}@hust.edu.cn).

S. Li and G. Caire are with the Electrical Engineering and Computer Science Department, Technische Universität Berlin, 10587 Berlin, Germany (e-mail: {shuangyang, caire}@tu-berlin.de).

In addition to the above studies, the application of FAS in practical wireless systems has also been developed and investigated. These include the fluid antenna multiple access [4], FAS and reconfigurable intelligent surfaces (RIS)-assisted beamforming [10], [11], FAS-assisted integrated sensing and communications [12], [13], FAS-assisted simultaneous wireless information and power transfer systems [14]. The effectiveness witnessed from these applications demonstrates the great potential of FAS in future wireless communications.

*Motivation of this paper:* The inherent frequency-space coupling phenomenon in wideband communication systems imposes fundamental limitations on conventional diversity schemes. Traditional half-wavelength antenna arrays fail to adequately mitigate severe frequency-selective fading effects, particularly those subcarriers exhibiting sub-noise floor gain [15]. This limitation stems primarily from their fixed spatial positions, especially when deployed in propagation environments featuring pronounced delay spread and rich multipath components. The electromagnetic equivalence between spatial displacement and temporal delay of path propagation reveals that sub-wavelength antenna repositioning can significantly reconfigure multipath interference patterns. The proposed FAS-assisted spatial equalization mechanism overcomes these challenges through real-time position adaptation within compact apertures, thereby providing enhanced interference suppression capability through extra spatial diversity before the traditional receiving process. However, two fundamental barriers hinder practical implementation:

- *Joint Frequency-Space Channel Estimation:* Leveraging the continuous space, FAS-assisted wireless systems surpass fixed half-wavelength arrays in new features. However, these applications fundamentally depend on full channel-state-information (CSI) knowledge, with FAS having an extra continuous space dimension in its CSI compared to conventional systems. This means that one should assess additional CSI utilizing the same data as the conventional methods have, leading to a technical challenge.
- *Real-Time Position Optimization for Spatial Equalization:* The combinatorial explosion inherent in optimal antenna positioning leads to high computation latency, as exhaustive search methods incur prohibitive computational complexity [16]–[18].

Recent efforts have explored compressed sensing and machine learning techniques to address the channel estimation. The electromagnetic analysis in [19] demonstrated that half-wavelength sampling schemes exhibit inherent deficiencies in achieving lossless channel reconstruction, thus mandating systematic oversampling approaches with adaptive interpolation to compensate for spectral leakage distortions. While Bayesian frameworks such as S-BAR [20] and LMMSE estimators [21] addressed estimation uncertainty, they introduced the computational complexity scaling with antenna dimensions. Moreover, most methods rely on restrictive assumptions about channel sparsity [22]–[24] or spatial correlation structures [25], [26], which may not hold in practical multi-user environments with mutual coupling effects.

As the key challenges lie in balancing reconstruction accuracy against frequency and space overhead and computational complexity, there is a critical need for an efficient es-

imation and optimization framework accounting for wireless propagation properties and intrinsic physical constraints. As shown in Fig. 1, this paper aims to solve the above question through a tripartite methodology:

- 1) *Recovery feasibility analysis:* Establishing the theoretical analysis for the recovery of frequency-space characteristics (FSC) from limited observations, ensuring that the problem is well-posed and solvable under specific conditions. We find that the physical aperture constraints in FAS induce leakage effects that degrade channel sparsity to a group-sparse structure, addressed by a novel convex optimization framework (CSOCP) minimizing  $\ell_1/\ell_2$ -mixed norms in delay-wavenumber domain. Theoretical tight recovery bounds under dictionary-adapted group RIP conditions are also proposed, rigorously guaranteeing precise frequency-space channel reconstruction.
- 2) *Channel estimation:* Developing a computationally efficient algorithm to accurately reconstruct FSC from compressed observations, leveraging advanced optimization techniques and prior knowledge of signal structure. Based on the leakage-aware group-sparse theory, the descending correlation group orthogonal matching pursuit (DC-GOMP) is proposed whose dynamic descending-order grouping mechanism replaces static leakage-based group selection. This framework fundamentally overcomes subcoherence limitations, achieving order-of-magnitude efficiency gains in solving CSOCP problems through descending-correlative group orthogonalization.
- 3) *Positions optimization:* Designing an algorithm to determine the optimal or near-optimal configuration of receiver positions, maximizing the performance of FSC recovery while minimizing resource utilization. We reformulate the max-min antenna position optimization of SE as a mixed-integer linear programming (MILP) problem with guaranteed global optimality by the branch-and-bound method. To enable the real-time implementation, we further propose greedy row selection with isolated preselection (GRSIP) algorithm, a low-complexity algorithm that maintains around 80% of optimal performance on average while reducing computation time by two orders of magnitude.

Simulation results indicate that, (i) the proposed DC-GOMP greatly outperforms the conventional OMP and GOMP in lower-power details of recovery and convergence rate; (ii) The SE framework demonstrates scalable performance improvements in both deep fading suppression and average SNR enhancement, with efficacy positively correlated to aperture size configurations.

The rest of this paper is organized as follows. Section II introduces the system model and formulation of channel estimation. In Section III, the key theoretical framework based on the fact of leakage has been established. Section IV gives the algorithms to perform the channel estimation and spatial estimation. In Section V, numerical results are provided, and the conclusion is drawn in Section VI.

*Notation:* The notation adopted in the paper is as follows. We use bold to denote matrices and vectors. Specifically,  $\mathbf{I}_N$  denotes the  $N \times N$  identity matrix.  $\{\cdot\}^T$  and  $\{\cdot\}^H$

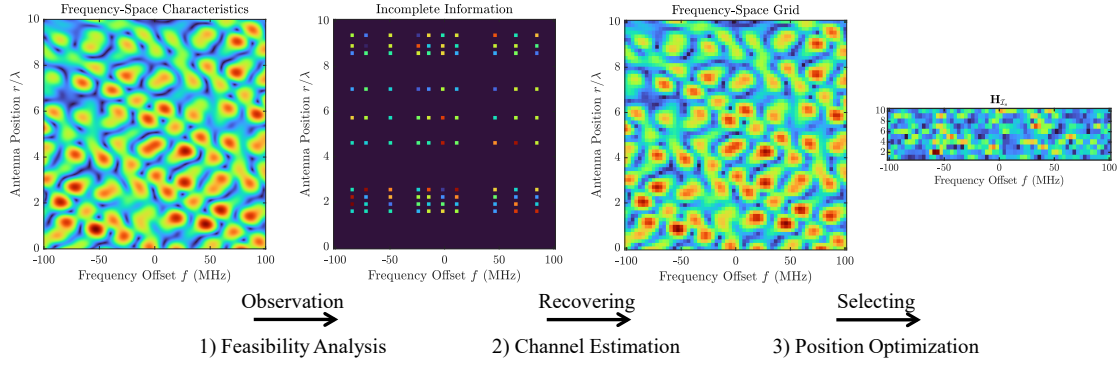


Figure 1. The tripartite methodology of this paper. (1) recovery feasibility analysis, (2) frequency-space channel estimation, and (3) positions optimization for spatial equalization.

denote the transpose, and the Hermitian operator.  $\{\mathbf{X}\}^\dagger$  is the Moore-Penrose pseudoinverse of  $\{\mathbf{X}\}$ .  $\hat{\mathbf{X}}$  and  $\hat{\mathbf{v}}$  denote the estimators of matrix  $\mathbf{X}$  and vector  $\mathbf{v}$ .  $\text{vec}(\cdot)$  denotes the vectorization of matrix.  $\text{blkdiag}\{\mathbf{A}_1, \dots, \mathbf{A}_N\}$  denotes a block diagonal matrix with  $\mathbf{A}_1, \dots, \mathbf{A}_N$  at the main diagonal.  $\text{Rank}\{\mathbf{X}\}$  and  $\text{tr}\{\mathbf{X}\}$  denote the rank and trace of matrix  $\mathbf{X}$ .  $\Re\{\cdot\}$  and  $\Im\{\cdot\}$  respectively denote the real and image part of a complex number.

## II. SYSTEM MODEL

In this section, we first provide the definition of the space-frequency characteristics (SFC) of FAS and its wide-band multipath propagation modeling in the space-frequency domain. Then we transform the SFC into the sparse wavenumber-delay domain and indicate the leaky phenomenon caused by limited aperture size and bandwidth. Then we propose the observation model with limited numbers of antennas and pilots. Finally, we propose the two-step framework for this model as depicted in Fig. 1, with the objective to maximize spatial diversity gain.

### A. Doubly-Selective Space-Frequency Characteristics

The SFC plays a critical role in designing the optimal antenna positions within a FAS. The wave propagation between two points comprises multiple propagation paths, each with distinct delays, angles, and signal strengths. Due to frequency dispersion, the propagation experiences varying delay combinations across different frequencies, leading to spectral selectivity. As an antenna moves within its available aperture—measured in units of the reference wavelength—the spectral selectivity undergoes significant variations. The SFC encapsulates all possible propagation modes between the regions  $\mathcal{S}_{tx}$  and  $\mathcal{S}_{rx}$  over the bandwidth  $\mathcal{B}$ , given specific boundary conditions and propagation environments. Fundamentally, it represents a simplified form of the Green's function, characterizing the system's response to different spatial and frequency-dependent variations.

**Definition 1 (SFC).** *The SFC represents the mapping from a compact transmit region  $\mathcal{S}_{tx} \subset \mathbb{R}^3$  to a compact receive region  $\mathcal{S}_{rx} \subset \mathbb{R}^3$  in a wireless communication system with spectral support  $\mathcal{B} \subset \mathbb{R}$ . It is defined as the kernel of a compact operator  $\mathcal{G}$ :*

$$(\mathcal{G}\mathbf{x})(\mathbf{p}_{rx}, \omega) = \int_{\mathcal{S}_{tx}} g(\mathbf{p}_{rx}, \mathbf{p}_{tx}, \omega) x(\mathbf{p}_{tx}, \omega) d\mathbf{p}_{tx}, \quad (1)$$

where  $\omega \in \mathcal{B}$  denotes angular frequency of the propagating wave,  $x(\mathbf{p}_{tx}, \omega) : \mathcal{S}_{tx} \times \mathcal{B} \rightarrow \mathbb{C}$  is the source density function.<sup>1</sup>  $\mathbf{p}_{rx} \in \mathcal{S}_{rx}$  denotes receiver coordinates.  $g(\mathbf{p}_{rx}, \mathbf{p}_{tx}, \omega)$  encodes wave propagation characteristics.

We consider the case that the transmitting region  $\mathcal{S}_{tx}$  has only one spatial point, the receiving region  $\mathcal{S}_{rx}$  consists of a line segment of a size  $|\mathcal{S}_{rx}| = W$ , and limited bandwidth  $\mathcal{B} = B$ . This allows us to simplify the notation  $x(\mathbf{p}_{tx}, \omega)$  as  $x(\omega)$ ; thus the general SFC function in (1) is reduced to

$$(\mathcal{G}x)(r, \omega) = g(r, \omega)x(\omega), \quad (2)$$

where  $\omega \in [-B/2, B/2]$  and  $r \in [0, W]$  represent the frequency and space components, respectively. Frequency dispersion is a phenomenon in which the propagation characteristics of a channel or medium vary with frequency, resulting in different frequency components traveling at distinct phase velocities or experiencing different attenuation levels. For a specific path from the fixed transmitting antenna (Tx) to the receiving antenna (Rx) with coordinate  $\mathbf{p}$ , its frequency response can be expressed as  $\alpha_l(\omega)e^{j(\mathbf{k}_l^T \mathbf{p} + \omega\tau_l)}$ . The attenuation that varies with frequency is typically taken into account in ultra-wideband wireless channels [27] [28]. In the case of wideband, we disregard the frequency-dependent attenuation for each path and only consider the frequency-dependent array manifold. The channel response from the fixed source point to a movable sink point at position  $r$  and frequency  $\omega$  can be expressed as

$$g(r, \omega) = \sum_l^L \alpha_l e^{j \frac{\omega + \omega_c}{c} (r \cos \theta_l + c\tau_l)}, \quad (3)$$

which presents the sum of  $L$  resolvable paths with different angle-of-arrival (AoA)  $\theta_l \in (0, \pi)$  and group delays  $\tau_l \in [0, \tau_{max}]$ . The complex attenuation  $\alpha_l$  is the result of the small scale fading that satisfy a uniform distribution within  $[0, 1]$ , i.e.,  $\Re\{\alpha_l\}, \Im\{\alpha_l\} \stackrel{\text{i.i.d.}}{\sim} \mathcal{N}(0, 1), \forall l$ . The  $\omega_c$  denotes the angular frequency of the central carrier.

Denote the number of considered discrete positions in  $[0, W]$  by  $M$ , and the number of considered discrete frequencies in  $[-B/2, B/2]$  by  $K$ . We obtain the discrete expression of  $g(r, \omega)$  by the resolutions of  $\Delta r \ll \lambda$  and  $\Delta \omega \leq 2\pi/\tau_{max}$  in the space and frequency domains<sup>2</sup> which is denoted as

<sup>1</sup>For example, in electromagnetic systems,  $x(\mathbf{p}_{tx}, \omega)$  represents current density ( $A/m^2$ ) or charge distribution ( $C/m^3$ )

<sup>2</sup> $\tau_{max}$  is the maximal delay spread of the wireless propagation.

space-frequency grid (SFG)  $\mathbf{G} \in \mathbb{C}^{M \times K}$ ,

$$\mathbf{G} = [\mathbf{g}_1, \mathbf{g}_2, \dots, \mathbf{g}_K] = [\bar{\mathbf{g}}_1, \bar{\mathbf{g}}_2, \dots, \bar{\mathbf{g}}_M]^T, \quad (4)$$

where the vector  $\mathbf{g}_k \in \mathbb{C}^{M \times 1}$  denotes the space-selective response at  $k$ -th frequency point  $(\frac{k}{K} - \frac{1}{2})B$ , and the  $m$ -th element of  $\mathbf{g}_k$  is  $\mathbf{g}_k(m) = g(\frac{m}{M}W, (\frac{k}{K} - \frac{1}{2})B)$ ; the vector  $\bar{\mathbf{g}}_m \in \mathbb{C}^{K \times 1}$  denotes the frequency-selective response at  $m$ -th location point in space domain.

### B. Sparse Representation in Wavenumber-Delay domain

For a FAS with finite aperture size and bandwidth, the SFG can be represented sparsely in the wavenumber-delay domain as Dirac-like functions with respect to wavenumber and delay of each path. Although different frequency components from each path have different phase shifts, they share the same angle-of-arrival (AoA) (i.e., they share the same angular support), which can be depicted as the expression in the wavenumber-frequency domain as

$$\tilde{g}(\mathbf{k}, \omega) = \sum_{l=1}^L \alpha_l e^{j(\omega + \omega_c)\tau_l} W \operatorname{sinc}\left(\frac{W(\omega + \omega_c)(\mathbf{k}_l - \mathbf{k})}{2c}\right),$$

where  $\mathbf{k}_l = \cos \theta_l$  and  $\theta_l$  denotes the wavenumber and the AoA of  $l$ -th path. By taking the Inverse Fourier Transform of  $\tilde{g}(\mathbf{k}, \omega)$  on  $\omega$ , we have the expression in the delay-wavenumber domain is

$$\tilde{\tilde{g}}(\mathbf{k}, \tau) \approx WB \sum_{l=1}^L \alpha_l e^{j\omega_c(\tau_l - \tau)} \Lambda_l(\mathbf{k}, \tau), \quad (5)$$

where the leakage pattern can be described as

$$\Lambda_l(\mathbf{k}, \tau) = \operatorname{sinc}\left(\frac{W(2\omega_c - B)(\mathbf{k}_l - \mathbf{k})}{4c}\right) \operatorname{sinc}\left(\frac{B(\tau_l - \tau)}{2}\right). \quad (6)$$

The leakage effect implies a degraded sparsity in the wavenumber domain [29]. To study this relationship, we consider the energy decay of the leakage pattern, given a specific path, the amplitude decay has the envelope  $|\Lambda_l(\mathbf{k}, \tau)| \leq \Lambda_l^{\text{env}}(\mathbf{k}, \tau) := 8c(WB(2\omega_c - B)|\mathbf{k}_l - \mathbf{k}||\tau_l - \tau|)^{-1}$ , where  $\tilde{\tilde{g}}(\mathbf{k}, \tau)$  can be considered as approximately sparse (or compressible) in the wavenumber domain [30]. As a result, a sparsity-degradation coefficient  $\gamma$  can be obtained as follows.

**Definition 2.** Given the aperture size  $W$  and bandwidth  $B$  of the FAS and the power detection threshold  $T$ . For an arbitrary frequency bin, the sparsity-degradation coefficient in wavenumber domain can be defined as

$$\gamma = \frac{|\{(\mathbf{k}, \tau) | \Lambda_l^{\text{env}}(\mathbf{k}, \tau)^2 \geq T\}|}{\Delta \mathbf{k} \Delta \tau}, \quad (7)$$

where  $\Delta \mathbf{k}$  and  $\Delta \tau$  denote the resolution of the sufficient grid of  $\tilde{\tilde{g}}(\mathbf{k}, \tau)$ . Normally,  $T$  is larger than the noise power  $\sigma_w^2$ .

From the propagation perspective, the sparsity of the wavenumber domain depends on the number of paths  $L$ . The support set of these paths is identical and corresponds to the set of indices in the wavenumber domain associated with each path, i.e.,  $\operatorname{supp}\{\tilde{\mathbf{g}}_k\} = \{\mathbf{k}_l/\mathbf{k}\}_L, \forall k$ . We can express the spatially-selective profile at  $k$ -th frequency point as

$$\mathbf{g}_k = \mathbf{A}(\omega_k) \tilde{\mathbf{g}}_k, \quad (8)$$

where the array manifold matrix  $\mathbf{A}(\omega_k) \in \mathbb{C}^{M \times M}$  maps the angular domain into the space domain,

$$\mathbf{A}(\omega_k) = [\mathbf{a}(\mathbf{k}_1; \omega_k), \mathbf{a}(\mathbf{k}_2; \omega_k), \dots, \mathbf{a}(\mathbf{k}_M; \omega_k)]. \quad (9)$$

Note that  $\{\mathbf{k}_q\}_M$  is the uniform sampling points in angular domain and  $\mathbf{a}(\mathbf{k}_l; \omega_k) \in \mathbb{C}^{M \times 1}$  is the frequency-dependent array manifold,

$$\mathbf{a}(\mathbf{k}; \omega_k) = \left[1, e^{j\frac{W(\omega_k + \omega_c)\mathbf{k}}{cM}}, \dots, e^{j\frac{(M-1)W(\omega_k + \omega_c)\mathbf{k}}{cM}}\right]^T. \quad (10)$$

Under the assumption of high space resolution, the array manifold matrix in (9) is actually the oversampled discrete Fourier transform (DFT) matrix in which the sampled frequencies are taken over at small intervals of varying lengths. This leads to an overcomplete frame whose columns are highly correlated, e.g.,  $\mathbf{a}(\mathbf{k}_m; \omega_k)^T \mathbf{a}(\mathbf{k}_{m-1}; \omega_k) \rightarrow 1$ .

The high coherence of the overcomplete frame and the leakage effect are fundamentally equivalent here, both arising from the inability of the aperture to achieve high angular resolution. This is analogous to the relationship between spectral bandwidth and sampling rate. When the sensing matrix (specifically, the array manifold matrix) exhibits high coherence, the resulting observations tend to be highly correlated. Consequently, this introduces significant ambiguities in distinguishing the precise sparse signal in high-resolution wavenumber-delay grid. Fortunately, in this paper, the recovery objective focuses on the SFG  $\mathbf{G}$  in frequency-space domain rather than  $\tilde{\mathbf{G}}$  or  $\tilde{\tilde{\mathbf{G}}}$ .

### C. Compressed Observation Model

Considering the propagation model of SFG and the intrinsic nature of the transformation, we give the noisy compressed observation model in this subsection. Let us consider the wideband SIMO system where the movable array has the initial set of antenna positions  $\mathcal{I}_r \subset \{1, 2, \dots, M\}$ ,  $|\mathcal{I}_r| = N_r$ , and inserted pilots have positions in the set  $\mathcal{I}_p \subset \{1, 2, \dots, K\}$ ,  $|\mathcal{I}_p| = N_p$ . The pilot located at the  $i \in \mathcal{I}_p$ -th frequency bin is denoted as  $s_i \in \mathbb{C}$ . Here we define the location-selecting matrix  $\mathbf{S}_{\mathcal{I}_r} \in \mathbb{C}^{N_r \times M}$  and the pilots-selecting matrix  $\mathbf{S}_{\mathcal{I}_p} \in \mathbb{C}^{N_p \times K}$  as

$$\begin{aligned} \mathbf{S}_{\mathcal{I}_r} &= [\mathbf{e}_{i_{r,1}}, \dots, \mathbf{e}_{i_{r,N_r}}]^T, i_{r,n} \in \mathcal{I}_r; \\ \mathbf{S}_{\mathcal{I}_p} &= [s_{i_{p,1}} \bar{\mathbf{e}}_{i_{p,1}}, \dots, s_{i_{p,N_p}} \bar{\mathbf{e}}_{i_{p,N_p}}]^T, i_{p,n} \in \mathcal{I}_p. \end{aligned} \quad (11)$$

Note that  $\mathbf{e}_{i_{r,n}}, n = 1, \dots, N_r$  (each with dimension  $M \times 1$ ) and  $\bar{\mathbf{e}}_{i_{c,n}}, n = 1, \dots, N_c$  (each with dimension  $K \times 1$ ) represent the  $n$ -th standard unit vectors, where the  $n$ -th element is 1 and all other elements are 0. We can model the available observations of SFG at the receiver as

$$\mathbf{Y}_m = \mathbf{S}_{\mathcal{I}_r} \mathbf{G} \mathbf{S}_{\mathcal{I}_p}^T + \mathbf{Z}, \quad (12)$$

where  $\mathbf{Z} \in \mathbb{C}^{N_r \times N_c}$  denotes the i.i.d. noise matrix with covariance matrix  $\sigma_w^2 \mathbf{I}$ , and  $\mathbf{Y}_m \in \mathbb{C}^{N_r \times N_c}$  denotes the incomplete observations of the SFG. Due to the frequency dispersion, the array manifold matrix varies as the frequency changes, and we need to apply the vectorization expression for all  $K$  frequency points within the bandwidth. We impose the operator  $\operatorname{vec}(\cdot)$  on both sides of (12),

$$\operatorname{vec}(\mathbf{Y}_m) = (\mathbf{S}_{\mathcal{I}_p} \otimes \mathbf{S}_{\mathcal{I}_r}) \operatorname{vec}(\mathbf{G}) + \mathbf{z}, \quad (13)$$

$$\underbrace{\text{vec}(\mathbf{Y}_m)}_{\mathbf{y}_0} = \underbrace{(\mathbf{S}_{\mathcal{I}_p} \otimes \mathbf{S}_{\mathcal{I}_r})}_{\mathbf{S}} \underbrace{\text{blkdiag}\{\mathbf{A}(\omega_1), \dots, \mathbf{A}(\omega_K)\}}_{\mathbf{D}} \underbrace{(\mathbf{F}^T \otimes \mathbf{I}_M)}_{\mathbf{M}} \underbrace{\text{vec}(\tilde{\mathbf{G}})}_{\mathbf{x}_0} + \mathbf{z} \quad (16)$$

where  $\otimes$  denotes the Kronecker product,  $\mathbf{z} \in \mathbb{C}^{N_r N_p \times 1}$  is the i.i.d. Gaussian noise vector, and the identical equation  $\text{vec}(\mathbf{C}) = \text{vec}(\mathbf{A}\mathbf{X}\mathbf{B}) = (\mathbf{B}^T \otimes \mathbf{A}) \text{vec}(\mathbf{X})$  is used. The frequency-space domain  $\text{vec}(\mathbf{G}) \in \mathbb{C}^{MK \times 1}$  can be expressed as the linear transform of the sparse matrix  $\tilde{\mathbf{G}} \in \mathbb{C}^{M \times K}$  in frequency-angular domain.

$$\text{vec}(\mathbf{G}) = \text{blkdiag}\{\mathbf{A}(\omega_1), \dots, \mathbf{A}(\omega_K)\} \text{vec}(\tilde{\mathbf{G}}). \quad (14)$$

Note that  $\tilde{\mathbf{G}} = \tilde{\mathbf{G}}\mathbf{F}$  where  $\mathbf{F}$  is the DFT matrix satisfying  $\mathbf{F}^H \mathbf{F} = \mathbf{I}_K$ . By  $\text{vec}(\mathbf{A}\mathbf{B}) = (\mathbf{B}^T \otimes \mathbf{I}_M) \text{vec}(\mathbf{A})$ , we have

$$\text{vec}(\tilde{\mathbf{G}}) = (\mathbf{F}^T \otimes \mathbf{I}_M) \text{vec}(\tilde{\mathbf{G}}). \quad (15)$$

Based on the compressed sensing process [31], we can model the relationship of observation, SFG and frequency-angular grid as (16), where  $\mathbf{y}_0 = \text{vec}(\mathbf{Y}_m) \in \mathbb{C}^{N_r N_c \times 1}$  denotes the observations,  $\mathbf{x}_0 = \text{vec}(\tilde{\mathbf{G}})$  denotes the sparse vector.  $\mathbf{S} = \mathbf{S}_{\mathcal{I}_p} \otimes \mathbf{S}_{\mathcal{I}_r} \in \mathbb{C}^{N_r N_c \times MK}$  and  $\mathbf{\Omega} = \text{blkdiag}\{\mathbf{A}(\omega_1), \dots, \mathbf{A}(\omega_K)\} \in \mathbb{C}^{MK \times MK}$ .  $\mathbf{\Psi} = (\mathbf{F}^T \otimes \mathbf{I}_M) \in \mathbb{C}^{MK \times MK}$  represents the DFT from the sparse delay-angular domains into group-sparse frequency-angular domain satisfying  $\mathbf{\Psi}^H \mathbf{\Psi} = \mathbf{I}_{MK}$ .

#### D. Two-Step Framework

We develop a two-step framework for the FAS-SIMO: first resolving space-frequency channel reconstruction through compressed sensing, then executing antenna position optimization to maximize spatial diversity gain.

**SFG Recovery.** The recovery of the SFG at the receiver is equivalent to the space-frequency channel estimation of the SIMO system with a FAS-assisted receiver. Due to the aperture limitation and the high demand of the angular/spatial resolution, as mentioned in Section II-B, the severe leakage effect and coherence between adjacent grid in SG are inevitable. Lemma 2 shows that  $\|\mathbf{\Psi}^H \mathbf{\Omega}^H \text{vec}(\mathbf{G})\|_2^2$  decays rapidly at the order of  $-2$ , and  $\mathbf{\Psi}^H \mathbf{\Omega}^H \mathbf{\Omega} \mathbf{\Psi}$  is a well-behaved block-diagonal sparse matrix.

In this study, we do not aim to recover the exact wireless propagation in wavenumber-delay domain but the SFC of FAS which can be sufficiently regarded as SFG (i.e.,  $\mathbf{G}$ ). We can obtain the estimated SFG  $\hat{\mathbf{G}}$  from the available observations in (12) by the method of  $\ell_1$ -analysis

$$\arg \min_{\mathbf{G} \in \mathbb{C}^{M \times K}} \|\mathbf{\Psi}^H \mathbf{\Omega}^H \text{vec}(\mathbf{G})\|_1 \quad (17a)$$

$$\text{s.t. } \|\mathbf{S} \text{vec}(\mathbf{G}) - \mathbf{y}_m\|_2 \leq \varepsilon, \quad (17b)$$

where  $\varepsilon$  denotes an upper bound on the noise level  $\sigma_\omega$ . The feasibility and stability of (17) have been analyzed, and more comprehensive conditions have been established to ensure the effective performance of the  $\ell_1$ -analysis [31].

**Location optimization.** In order to mitigate deep fading, we obtain the optimal positions  $\mathcal{I}_s$  to maximize the gain

of the subcarrier with the minimal power by the recovered SFG. The wideband receiving signal can be expressed as

$$\mathbf{H}_{\mathcal{I}_s} = [\bar{\mathbf{g}}_{i_1}, \bar{\mathbf{g}}_{i_2}, \dots, \bar{\mathbf{g}}_{i_{N_r}}]^T = [\mathbf{h}_1, \mathbf{h}_2, \dots, \mathbf{h}_K], \quad (18)$$

where  $\mathbf{H}_{\mathcal{I}_s} \in \mathbb{C}^{N_r \times K}$  and  $i_n \in \mathcal{I}_s$ . The  $k$ -th subcarrier of receiving signal can be expressed as

$$y_k = \mathbf{w}_k^H (\mathbf{h}_k x_k + \mathbf{z}), \quad (19)$$

where  $\mathbf{w}_k \in \mathbb{C}^{N_r \times K}$  is the combining weights of  $k$ -th subcarrier and  $\mathbf{h}_k$  is the  $k$ -th column of  $\mathbf{H}_{\mathcal{I}_s}$ . The  $n$ -th row of  $\mathbf{H}_{\mathcal{I}_s}$  (i.e.,  $\bar{\mathbf{g}}_{i_n}$ ) is equal to  $i_n$ -th row of  $\tilde{\mathbf{G}}$ . The  $\mathcal{I}_s^{\text{opt}}$  can be obtained by

$$\arg \max_{\mathcal{I}_s} \min_k \rho_k \quad (20a)$$

$$\text{s.t. } \rho_k = \mathbb{E}\{|\mathbf{w}_k^H \mathbf{h}_k x_k|^2\} / \mathbb{E}\{|\mathbf{w}_k^H \mathbf{z}|^2\}, \quad (20b)$$

$$h_{k, i_n} = G_{i_n, k}, \quad i_n \in \mathcal{I}_s, \quad (20c)$$

$$|\mathcal{I}_s| = N_r, \quad \mathcal{I}_s \subset \{1, \dots, M\}, \quad (20d)$$

where  $G_{i_n, k}$  is the entries of  $\tilde{\mathbf{G}}$  at  $i_n$ -th row and  $k$ -th column ( $k \in \{1, \dots, K\}$ ), and  $\rho_k$  is the average SNR of the  $k$ -th subcarrier. To counteract the selectivity and guarantee the robustness of the transmission, we apply the MRC for  $k$ -th subcarrier along with each antenna, i.e.,  $\mathbf{w}_k = \mathbf{h}_k$ .

### III. CHANNEL ESTIMATION BASED ON GROUP SPARSITY

This section first presents a theoretical analysis of error bounds for group sparsity recovery of SFG. Under the noisy environments with leakage effects, sparse signal recovery faces two critical challenges: (i) the degradation of sparsity in the delay-angle domain due to leakage, where non-zero elements cluster into group structures, and (ii) the coherence of the measurement matrix  $\mathbf{M}$ , which destabilizes recovery. To analyze the feasibility, we introduce the D-GRIP and establish a rigorous upper bound on the SFG recovery error. This bound depicts the relationship between recovery error, group sparsity level  $k$ , number of observations  $N_r N_p$ , and dictionary redundancy. Furthermore, we define group coherence  $\mu_{\mathcal{J}}$  and sub-coherence  $\nu$ , and characterize the group structure under leakage effects and derive a theoretical upper bound on group size  $\gamma$ , providing theoretical guidelines for designing channel estimation algorithms.

Subsequently, we design an efficient and robust algorithm, called *descending correlation group orthogonal matching pursuit* (DC-GOMP), based on the group sparsity and the fact that the subcoherence inside one leakage group is high.

#### A. Error Bound of Group Sparsity Recovery

We use the model in (16) to explain the concept of group sparsity. The noisy observation model is

$$\mathbf{y}_0 = \mathbf{M}\mathbf{x}_0 + \mathbf{z} = \mathbf{S}\mathbf{g}_0 + \mathbf{z} = \mathbf{S}\mathbf{D}\mathbf{x}_0 + \mathbf{z}, \quad (21)$$

where  $\mathbf{M} = \mathbf{S}\mathbf{D} = \mathbf{S}\mathbf{\Omega}\mathbf{\Psi} \in \mathbb{C}^{N_r N_c \times MK}$  with  $N_r N_c \ll MK$ , and  $\mathbf{x}_0$  denotes vectorized sparse expression in the

wavenumber-delay domain. From the perspective of propagation,  $\mathbf{x}_0$  should be  $L$ -sparse corresponding to the number of paths. Nonetheless, as outlined in Section II-B, the leakage effect diminishes its sparsity characterized by a factor  $\gamma$ , resulting in  $\gamma L$  non-zero elements emerging in groups. Let  $\mathcal{J} \triangleq \{\mathcal{I}_j\}_{j=1}^J$  be a partition of the set  $\{1, \dots, MK\}$ , i.e.,  $\bigcup_{j=1}^J \mathcal{I}_j = \{1, \dots, MK\}$  and  $\sum_{j=1}^J |\mathcal{I}_j| = MK$ . We assign the size of each group  $|\mathcal{I}_j| = \gamma$  to match the sparsity degradation. For the  $\mathbf{x}_0 \in \mathbb{C}^{MK \times 1}$  and  $\mathbf{M} \in \mathbb{C}^{N_r N_c \times MK}$ , we define the  $j$ -th subvector of size  $\gamma \times 1$

$$\mathbf{x}_0[j] = [\tilde{x}_i : i \in \mathcal{I}_j]^T, \quad (22)$$

and  $j$ -th column-group of size  $N_r N_c \times \gamma$

$$\mathbf{M}[j] = [\mathbf{m}_i : i \in \mathcal{I}_j], \quad (23)$$

where  $\mathbf{m}_i$  is the  $i$ -th column of  $\mathbf{M}$ . A vector  $\mathbf{x}_0$  is called *group  $L$ -sparse* as the condition  $\sum_{j=1}^J I(\|\mathbf{x}_0[j]\|_2) \leq L$  holds, where  $I(\cdot)$  is the indicator function.

By defining the  $\ell_1/\ell_2$ -norm  $\|\cdot\|_{2,\mathcal{J}}$  where  $\|\mathbf{x}_0\|_{2,\mathcal{J}} = \sum_{j=1}^J \|\mathbf{x}_0[j]\|_2$ , we now rewrite the optimization problem in (17) as the convex second-order cone program

$$\hat{\mathbf{g}} = \arg \min_{\mathbf{g} \in \mathbb{C}^{MK \times 1}} \|\mathbf{D}^H \mathbf{g}\|_{2,\mathcal{J}} \quad (24a)$$

$$\text{s.t. } \|\mathbf{S} \mathbf{g} - \mathbf{y}_0\|_2 \leq \varepsilon. \quad (24b)$$

We will then impose a natural group property on the sampling matrix  $\mathbf{S}$ , analogous to the group restricted isometry property defined in [31], [32].

**Definition 3.** (*D-GRIP*) Let  $\Sigma_k$  be the space spanned by given dictionaries  $\mathbf{D}$  and group  $k$ -sparse vector  $\mathbf{x}$ , i.e.,  $\mathbf{D}\mathbf{x} \in \Sigma_k$ ,  $\forall \mathbf{x}$ , s.t.  $\|\mathbf{x}\|_{2,0,\mathcal{J}} \leq k$ . The sampling matrix  $\mathbf{S}$  is said to obey the group restricted isometry property adapted to  $\mathbf{D}$  (abbreviated *D-GRIP*) with constant  $\delta_k$  if

$$(1 - \delta_k) \|\mathbf{v}\|_2^2 \leq \|\mathbf{S}\mathbf{v}\|_2^2 \leq (1 + \delta_k) \|\mathbf{v}\|_2^2 \quad (25)$$

holds for all  $\mathbf{v} \in \Sigma_k$ .

We point out that  $\Sigma_k$  is just the image under  $\mathbf{D}$  of all group  $k$ -sparse vectors. The *D-GRIP* degenerates into standard RIP when  $\mathbf{D} = \mathbf{I}$  [33].

**Theorem 1.** (*Error Bound*) Let  $\mathbf{y}_0 = \mathbf{S}\mathbf{g}_0 + \mathbf{z} = \mathbf{S}\mathbf{D}\mathbf{x}_0 + \mathbf{z}$  be noisy observations of a Group  $k$ -sparse vector and  $\mathbf{D}$  is an arbitrary tight frame. Let  $\hat{\mathbf{g}}$  be a solution to (24) and  $(\mathbf{D}^H \mathbf{g}_0)^{(k)}$  be the largest group  $k$ -sparse approximation of  $\mathbf{D}^H \mathbf{g}_0$ . If  $\mathbf{S}$  satisfies the *D-GRIP* with  $\delta_{k+P} < 1$  then

$$\|\hat{\mathbf{g}} - \mathbf{g}_0\|_2 \leq C_0 \|\mathbf{D}^H \mathbf{g}_0 - (\mathbf{D}^H \mathbf{g}_0)^{(k)}\|_{2,\mathcal{J}} + C_1 \varepsilon, \quad (26)$$

where

$$C_0 = 2 \frac{a\sqrt{1 - \delta_{k+P}} + \sqrt{1 + \delta_P}}{b\sqrt{1 - \delta_{k+P}} - \sqrt{1 + \delta_P}}, \quad (27)$$

$$C_1 = \frac{2}{b\sqrt{\rho}\sqrt{1 - \delta_{k+P}} - \sqrt{1 + \delta_P}}, \quad (28)$$

and  $a = \sqrt{1 + \frac{1}{c}}$ ,  $b = \sqrt{\frac{1}{\rho} - 1 - c}$ ,  $\rho = k/P$ , with the positive number  $c$ .

*Proof:* The proof of Theorem 1 is inspired by both the result of compressed sensing with redundant dictionaries [31]

and the robust recovery of block sparse vector [32]. The new challenge here is that, rather than bounding the error  $\|\hat{\mathbf{x}} - \mathbf{x}_0\|_2$  in group sparse domain with related to the mixed norm  $\|\cdot\|_{2,\mathcal{J}}$ , we try to bound the image error  $\|\hat{\mathbf{g}} - \mathbf{g}_0\|_2$  under the projection  $\mathbf{D}$ . By bounding the group tail of  $\|\mathbf{D}^H(\hat{\mathbf{g}} - \mathbf{g}_0)\|_2$  (step 1) and the application of the *D-GRIP* (step 2), we finally obtain the expression of the error bound (step 4). See Appendix A for the details. ■

Theorem 1 provides theoretical support for the SFG recovery problem by noting the group sparsity of SFG in the delay-angular domain. Given the number of observations  $N_r$  and  $N_p$ , the upper bound of recovery error is linked to the tail power  $\|\mathbf{D}^H \mathbf{g}_0 - (\mathbf{D}^H \mathbf{g}_0)^{(k)}\|_{2,\mathcal{J}}$ , noise power  $\varepsilon$ , or group sparsity  $k$ . This emphasizes choosing the correct group support for effective recovery, leading to a group-based algorithm proposed later. As the number of observations grows, the group restricted isometry constant adapted to  $\mathbf{D}$  (i.e.,  $\delta_k$ ) decreases, reducing the error bound. In the absence of noise and leakage,  $\ell_1/\ell_2$ -norm minimization or traditional greedy algorithms can accurately solve the problem in (24). However, noise and restricted aperture size and bandwidth prevent perfect recovery.

The upper bound on the error established in Theorem 1 confirms that the problem (24) is feasible under the proper *D-GRIP* condition. However, the actual recovery error is highly dependent on the specific recovery algorithm employed. Unlike conventional sparse recovery or channel estimation, which aims for precise parameter estimation, our primary objective is to reconstruct the SFG, thereby simplifying the problem. In environments with a large number of propagation paths, the limited aperture size and bandwidth constrain the number of resolvable paths, which is often smaller than the actual number of physical paths. Paths that are close in the wavenumber-delay domain tend to merge due to leakage effects, resulting in indistinguishable components at the system level. Nevertheless, this negative effect can be mitigated since our recovery object is the expression in space-frequency domain rather than wavenumber-delay domain. This distinction motivates the development of more targeted algorithms, which will be introduced in Section III-C.

## B. Leakage and Group Coherence

The coherence of a dictionary measures the similarity between its columns [34]. Since computing the restricted isometry constants of a given matrix is an NP-hard problem, coherence-based methods are proposed to characterize the recovery capabilities of both the recovery algorithm and the measurement matrix [35], [36]. The coherence in the general sense is defined as  $\mu = \max_{i \neq j} |\mathbf{m}_i^H \mathbf{m}_j|$ ,  $\forall i, j \in \{1, \dots, MK\}$ . However, the nonzero entries do not appear randomly across all possible positions; instead, they exhibit a structured grouping pattern. The *group-coherence* is therefore defined as the maximum singular value of the correlation matrix between each pair of column groups, i.e.,

$$\mu_{\mathcal{J}} = \max_{i,j \in \{1, \dots, MK\}; i \neq j} \frac{1}{\gamma} \rho(\mathbf{M}^H[i] \mathbf{M}[j]), \quad (29)$$

where  $\rho(\mathbf{A}) = \sqrt{\lambda_{\max}(\mathbf{A}^H \mathbf{A})}$ , and recall that  $\mathcal{J} \triangleq \{\mathcal{I}_j\}_{j=1}^J$ ,  $\mu_B = \mu$  as  $\gamma = 1$ . The local property characterized

by the *sub-coherence* of  $\mathbf{M}$  is defined as

$$\nu = \max_{j \in \{1, \dots, J\}} \max_{n \neq m: \mathbf{m}_n, \mathbf{m}_m \in \mathbf{M}[j]} |\mathbf{m}_n^H \mathbf{m}_m|. \quad (30)$$

The aforementioned types of coherence pertain to global and local characteristics, respectively. Technically, the support of leakage is an ellipse-like region in the delay-angular grid. For the ease of computation and grouping, we can express the leakage in the delay domain and wavenumber domain separately by relaxing the support into rectangles.

**Lemma 1.** *The sparsity degradation coefficient corresponds to the count of grid samples within the leakage region. Given the bandwidth  $B$ , the aperture size  $W$ , the carrier frequency  $\omega_c$ , the resolutions of the delay domain  $\Delta\tau$ , and the wavenumber domain  $\Delta\mathbf{k}_\theta$ , we have*

$$\gamma \leq \frac{32c}{\Delta\tau \Delta\mathbf{k}_\theta T B W (2\omega_c - B)}. \quad (31)$$

*Proof:* See Appendix B for the detailed proof.

**Remark 1.** *The number of paths  $L$  of the channel can be regarded as the group sparsity of the observation model in (21), which means that  $\mathbf{x}_0$  is a group  $L$ -sparse vector. The size of the group is offered by the sparsity degradation coefficient  $\gamma$  as given in Lemma 1.*

Lemma 1 provides guidance for choosing the group size in algorithms focused on group sparsity recovery. It indicates that increased bandwidth and aperture size notably reduce the sparsity degradation, aligning with our intuition. If there is no prior knowledge about the group-sparsity structure,  $\mathbf{x}_0$  will be treated as a  $\gamma L$ -sparse vector. Such that a sufficient condition for perfect recovery using OMP or  $\ell_1$  norm minimization is  $\gamma L < (\mu^{-1} + 1)/2$  where  $\mu$  is the conventional coherence of  $\mathbf{M}$  [34]. With the group structure, the sufficient condition can be replaced by a weaker one  $\gamma L < (\mu_{\mathcal{J}}^{-1} + \gamma - (\gamma - 1)\nu\mu_{\mathcal{J}}^{-1})/2$ , where the group-coherence and subcoherence are defined in (29) and (30) [37].

**Theorem 2.** *Given the delay spread  $\tau_{\max}$  of the channel, the bandwidth  $B = \beta\omega_c$ , the aperture size  $W = N_\lambda\lambda_c$  of FAS, and the size of SFG  $M, K$ , then we can respectively obtain two leakage coefficients in the delay domain and wavenumber domain*

$$\gamma_\tau = \frac{4K}{\tau_{\max} B \sqrt{T}}, \quad (32)$$

$$\gamma_{\mathbf{k}} = \frac{2M}{\pi \sqrt{T} N_\lambda (2 - \beta)}, \quad (33)$$

where  $T$  is the power detection threshold, and  $N_\lambda$  denotes the multiple of the wavelength.

*Proof:* See Appendix B for the detailed proof.

Theorem 2 further quantifies leakage coefficients in delay and wavenumber domains, linking them to system parameters such as bandwidth  $B$ , aperture size  $W$  and spread delay  $\tau_{\max}$ .  $\tau_{\max} B$  denotes the bandwidth-delay product, which is commonly used to characterize the number of independent paths that can be provided in the delay-frequency domain.  $N_\lambda$  represents the multiplicity of wavelengths that determines the ability to discern separate spatial paths. Higher  $\tau_{\max} B$  or  $N_\lambda$  leads to decreasing of the corresponding

sparsity degradations when the resolution is fixed. The power threshold usually depends on the noisy level as

$$T = \begin{cases} \frac{1}{2}, & \sigma_\omega^2 < 0.5; \\ \sigma_\omega^2, & \sigma_\omega^2 \geq 0.5. \end{cases} \quad (34)$$

Assuming that  $\Delta\omega = \frac{2\pi}{\tau_{\max}}$ , we have  $\Delta\tau = \frac{2\pi}{B}$ , since  $\frac{B}{\Delta\omega} = \frac{\tau_{\max}}{\Delta\tau} = K$ . Combining with  $\text{sinc}(B(\tau_l - \tau)/2)$  in (6), we have that there is no leakage related to  $\tau$ . Taking the half-power threshold (i.e.,  $T = 1/2$ ), we have

$$\gamma \leq \frac{2\sqrt{2}\omega_c M}{\pi N_\lambda (2\omega_c - B)}, \quad (35)$$

where  $W = N_\lambda\lambda$ . For the narrow band system, (35) can be simplified as  $\gamma \leq \sqrt{2}M/N_\lambda\pi$ .

To conclude, the analysis in this subsection lays the foundation for robust SFG recovery in scenarios with high matrix coherence and limited observations. It also underscores the importance of group-aware algorithms in mitigating sparsity degradation caused by leakage effects.

### C. DC-GOMP for Channel Estimation

As analyzed in Section III-A, traditional sparse recovery algorithms suffer severe performance degradation in frequency-space grid reconstruction due to two inherent limitations: 1) the high redundancy of over-complete dictionaries, and 2) spectral leakage induced by finite aperture size and bandwidth constraints. These limitations are empirically validated by the upper subfigures in Fig. 2, where conventional methods exhibit significant reconstruction errors. The orthogonal matching pursuit (OMP) algorithm, while theoretically guaranteeing sparse signal recovery through iterative residual correlation maximization and orthogonal projection updates, proves inadequate for dense scattering channels. Specifically, when resolving closely spaced multipath components (common in such environments), OMP tends to over-suppress adjacent paths after selecting a dominant component, as evidenced by missing grid points in Fig. 2(a). Moreover, its fixed iteration-depth requirement – mandating prior knowledge of path count – limits adaptability to varying channel conditions. To exploit structured sparsity, the group OMP (GOMP) algorithm extends OMP by replacing single-atom selection with group-wise subtraction based on predefined 2D-chunking partitions of the index set  $\{1, \dots, MK\}$ . This strategy improves leakage effect recovery in delay-wavenumber domains, as shown in Fig. 2(b)'s tighter support set concentration. However, GOMP's uniform grouping – adopted due to absent prior path distribution knowledge – fails to address intra-group energy misallocation caused by high subcoherence  $\nu$  (defined in (30)). Consequently, it delivers suboptimal space-frequency gain (SFG) recovery accuracy, as residual energy within erroneously grouped atoms persists through iterations.

The proposed Descending Correlation Group Orthogonal Matching Pursuit (DC-GOMP) algorithm operates by iteratively recovering dominant components of doubly-faded signals in the frequency-space domain. The algorithm initializes with the observed signal  $\mathbf{y}_0$ , sensing matrix  $\mathbf{M}$ , sparsifying transform  $\mathbf{D}$ , and parameters including maximum iteration count  $N_{\text{iter}}$ , selection cardinality  $\gamma = \gamma_\tau \gamma_{\mathbf{k}}$ , and residual threshold  $\varepsilon_1$ . Starting with an empty support set  $T_{(0)}$  and

initial residual  $\mathbf{r}_{(0)} = \mathbf{y}_0$ , the iterative process begins. At each iteration  $l$ , the correlation vector  $\mathbf{q} = \mathbf{M}^H \mathbf{r}_{(l-1)}$  is computed to quantify the alignment between the residual and dictionary atoms. The top- $\gamma$  indices  $\mathcal{I}_l$  corresponding to the largest magnitudes in  $\mathbf{q}$  are selected, breaking away from traditional leakage-constrained grouping to prioritize high-energy bases across delay-wavenumber subspaces. The support set is then updated as  $T_{(l)} = T_{(l-1)} \cup \mathcal{I}_l$ , and the sparse coefficients  $\mathbf{x}_{T_{(l)}}$  are estimated via least-squares minimization using the pseudo-inverse of the submatrix  $\mathbf{M}_{T_{(l)}}^\dagger$ . The residual  $\mathbf{r}_{(l)}$  is recalculated by subtracting the contribution of the estimated components, and the signal  $\hat{\mathbf{g}}_{(l)}$  in the fading domain is reconstructed through  $\mathbf{D}\hat{\mathbf{x}}_{(l)}$ . The process terminates when the residual norm falls below  $\varepsilon_1$  or the iteration limit is reached.

DC-GOMP addresses challenges in doubly-faded signal recovery through three pivotal design principles. First, its dynamic descending-order grouping mechanism replaces static leakage-based group selection with adaptive cross-subspace atom selection, reducing sub-coherence effects and preventing energy misallocation. By greedily selecting the  $\gamma$  most correlated atoms in each iteration, the algorithm rapidly captures dominant scattering features, with empirical results demonstrating that 80% of the signal energy is typically recovered within 20% of the total iterations (see Fig. 5). Second, the strategy inherently suppresses both group coherence  $\mu_{\mathcal{J}}$  and sub-coherence  $\nu$ , relaxing the theoretical recovery condition to  $\gamma L < \frac{1}{2}(\mu_{\mathcal{J}}^{-1} + \gamma - (\gamma - 1)\nu\mu_{\mathcal{J}}^{-1})$ . This ensures robustness under practical constraints such as dictionary redundancy and limited aperture/bandwidth-induced leakage. Crucially, DC-GOMP shifts the recovery objective from exact support identification in 2D-sparse domains to direct fidelity optimization in the doubly-fading domain (i.e., space-frequency domain), bypassing the computational complexity of traditional sparse recovery and the emergence of leaky dense paths. The resultant framework achieves a provable balance between reconstruction accuracy and computational efficiency, making it particularly suitable for large-scale systems with high spatial resolution requirements.

---

**Algorithm 1** DC-GOMP: Descending Correlation Group Orthogonal Matching Pursuit.

---

**Require:**  $\mathbf{S}, \mathbf{D}, \mathbf{M}, \mathbf{y}_0, N_{\text{iter}}, \gamma_\tau, \gamma_{\mathbf{k}}, \varepsilon_1$

**Ensure:**  $\hat{\mathbf{g}}$

- 1: Initialize:  $l = 0$ ,  $\mathbf{r}_{(0)} = \mathbf{y}_0$ ,  $\gamma = \gamma_\tau \gamma_{\mathbf{k}}$ ,  $T_{(0)} = \{\emptyset\}$
  - 2: **while**  $\|\mathbf{S}\hat{\mathbf{g}}_{(l)} - \mathbf{y}_0\|_2 > \varepsilon_1$  **and**  $l \leq N_{\text{iter}}$  **do**
  - 3:      $l = l + 1$
  - 4:      $\mathbf{q} = \mathbf{M}^H \mathbf{r}_{(l-1)}$ , where  $q_{i_n}$  is the  $i_n$ -th entry of  $\mathbf{q}$
  - 5:     sort  $\{i_n\}_n^{MK}$  in descending,  $q_{i_1} \geq q_{i_2} \cdots \geq q_{i_{MK}}$
  - 6:      $\mathcal{I}_l = \{i_1, i_2, \dots, i_\gamma\}$
  - 7:      $T_{(l)} = T_{(l-1)} \cup \mathcal{I}_l$ ,
  - 8:      $\mathbf{x}_{T_{(l)}} = \mathbf{M}_{T_{(l)}}^\dagger \mathbf{y}_0$
  - 9:      $\mathbf{r}_{(l)} = \mathbf{y}_0 - \mathbf{M}\mathbf{x}_{T_{(l)}}$
  - 10:      $\mathbf{x}_{T_{(l)}} \xrightarrow{T_{(l)}} \hat{\mathbf{x}}_{(l)}$
  - 11:      $\hat{\mathbf{g}}_{(l)} = \mathbf{D}\hat{\mathbf{x}}_{(l)}$
  - 12: **end while**
  - 13: **return**  $\hat{\mathbf{g}} = \hat{\mathbf{g}}_{(l)}$
- 

## IV. SPATIAL EQUALIZATION

After the SFG reconstruction on the receiver side, the receiver then needs to optimize the antenna positions. In this section, we reformulate the max-min antenna position optimization of SE in (20) as a mixed-integer linear programming (MILP) problem with guaranteed global optimality by the method branch-and-bound. To enable the real-time implementation, we reduce the computational complexity by further proposing a greedy row selection with isolated preselection (GRSIP) algorithm, which maintains decent performance in average while reducing the computation time by two orders of magnitude.

The problem in (20) can be rewritten as

$$\arg \max_{\mathcal{I}_s} \min_{k \in \{1, \dots, K\}} \|\mathbf{h}_k\|_2^2 \quad (36a)$$

$$\text{s.t. } h_{k,n} = G_{i_n,k}, i_n \in \mathcal{I}_s, \quad (36b)$$

$$|\mathcal{I}_s| = N_r, \mathcal{I}_s \subset \{1, \dots, M\}, \quad (36c)$$

where  $h_{k,n}$  denotes the  $n$ -th entry of  $\mathbf{h}_k$ . (36) is a max-min problem with the objective to maximize the minimum of the squares of the  $\ell_2$  norm of the individual column vectors  $\mathbf{h}_k$ . The constraints impose that the set  $\mathcal{I}_s$  is of size  $N_r$  and each  $\mathbf{h}_k$  is a vector of size  $N_r$  consisting of the elements in the set of selected row indices of the original matrix  $\mathbf{G}$ . Specifically, the  $n$ -th element of  $\mathbf{h}_k$  is the element of the  $k$ -th column and the  $i_n$ -th row of  $\mathbf{G}$ .

The index selection problems are typically formulated as integer programming problems. To solve such problems efficiently, it is often necessary to reformulate them as linear or mixed-integer programming models. However, the objective function in this case involves maximizing the minimum value, which presents a challenge due to its segmented and nonlinear nature. In integer programming, decision variables are generally binary, representing whether a specific row index is selected. Let  $p_i$  be a binary variable for  $i = 1, \dots, M$ , where  $p_i = 1$  indicates that the  $i$ -th row is selected, and  $p_i = 0$  indicates that it is not. Since exactly  $N_r$  rows must be selected, the constraint is given by  $\sum_{i=1}^M p_i = N_r$ . Since each vector  $\mathbf{h}_k$  is formed by  $k$ -th elements of the selected rows of  $\mathbf{G}$  we have

$$\|\mathbf{h}_k\|_2^2 = \sum_{i=1}^M p_i \cdot |G_{i,k}|^2. \quad (37)$$

The objective is to maximize the minimum value of  $\|\mathbf{h}_k\|_2^2$  over all  $k \in \{1, \dots, K\}$ . In other words, the problem is to maximize  $t$ , such that for all  $k$ ,  $\sum_{i=1}^M p_i \cdot |G_{i,k}|^2 \geq t$ .

This transforms the problem (36) into a mixed-integer linear programming (MILP) problem, where the objective is to maximize  $t$ , i.e.,

$$\arg \min_{\mathbf{p} \in \{0,1\}^{M \times 1}} -t \quad (38a)$$

$$\text{s.t. } \mathbf{p}^T \mathbf{g}_k^{\text{abs}} \geq t, \forall k \in \{1, 2, \dots, K\} \quad (38b)$$

$$\|\mathbf{p}\|_0 = N_r, \quad (38c)$$

$$t \geq 0, \quad (38d)$$

where the entries of  $\mathbf{g}_k^{\text{abs}} \in \mathbb{R}^{M \times 1}$  are the entries of  $\mathbf{g}_k \in \mathbb{C}^{M \times 1}$  in absolute value. With linear constraints, the problem (36) can be formulated as a linear integer programming problem (38).



The key advance of the MILP model is its global optimality guarantee, since it can explore all possible combinations via branch-and-bound. Furthermore, by employing upper and lower bound pruning strategies, MILP significantly reduces ineffective search efforts, thereby enhancing computational efficiency and guaranteeing the identification of the global optimality. However, despite its global optimality, its computational complexity still grows rapidly as the problem size increases with the time complexity  $\mathcal{O}(2^M \cdot K)$ . Empirical results show that when  $M > 50$  and  $K > 100$ , the size of the branch-and-bound search tree leads to memory and time costs that exceed practical limits.

---

**Algorithm 2** GRSIP: Greedy Row Selection with Isolated Preselection.

---

**Require:**  $\mathbf{G}$ ,  $N_r$ ,  $N_{\text{init}}$ ,  $\Delta n$

**Ensure:**  $\mathcal{I}_s$

```

1: Initialize:  $l = 0$ ,  $T_{(0)} = \{\emptyset\}$ 
2: while  $l \leq N_{\text{init}}$  do
3:    $i = \arg \max_{i \in T_{(l)}^c} \bar{\mathbf{g}}_i$ , s. t.  $D_1(\{i\}, T_{(l)}) \leq \Delta n$ 
4:    $l = l + 1$ 
5:    $T_{(l)} = T_{(l)} \cup \{i\}$ 
6: end while
7: while  $l \leq N_r$  do
8:    $i = \arg \max_{i \in T_{(l)}^c} \min_k \|\mathbf{h}_k\|_2$ , s. t.  $\mathbf{h}_k \in \text{Col}(\mathbf{H}_{T_{(l)} \cup \{i\}})$ 
9:    $l = l + 1$ 
10:   $T_{(l)} = T_{(l)} \cup \{i\}$ 
11: end while
12: return  $\mathcal{I}_s = T_{(l)}$ 

```

---

Hence, in the following we also propose a greedy algorithm in Algorithm 2 with the time complexity  $\mathcal{O}(MKN_r)$ . The algorithm starts by choosing  $N_{\text{init}}$  positions with the top average channel gains for each subcarrier, maintaining a minimum separation of  $\Delta n$  between them, where  $D_1(\cdot, \cdot)$  represents the minimal  $\ell_1$ -norm distance between two point

sets. Then it incrementally adds indices to the candidate set, following the principle of maximizing the minimum subcarrier gain, until  $N_r$  positions are chosen. Note that  $\mathbf{H}_T$  is formed by the row vectors of  $\mathbf{G}$  associated with row indices in  $T$ .

**Remark 2** (Applications to Other Models). *The theoretical analysis and algorithms of the two-step framework for FAS proposed in this work could be extended to other problems besides FAS. First, the proposed two-step framework could be directly extended to the antenna selection problem with discrete positions, regardless of whether the exact antennas deployment [38]–[41]. The group-sparse recovery formulation and D-GRIP analysis can be directly adapted to delay-Doppler domain channel estimation [42], [43], where structures induce similar group-wise sparsity patterns in reconstruction. The DC-GOMP algorithm employs a correlation-aware selection mechanism to dynamically resolve coherence conflicts, offering a systematic and efficient approach to sparse event detection. Then, MILP-based spatial equalization offers new insights for the resource-constrained optimization in RIS configuration on discrete phase [44]. These potential extensions highlight that our methodology effectively tackles the unified challenge of sparsity-aware optimization under structured constraints, making it applicable to a wide range of domains, including computational sensing, adaptive control, and beyond.*

## V. SIMULATION RESULTS

In this section, we present the performance of the proposed group-sparsity based frequency-space channel estimation algorithm, i.e., DC-GOMP, in comparison to two traditional algorithms (OMP, GOMP), under FAS-assisted wideband SIMO system. The proposed positions optimization methods, i.e., MILP and GRSIP, are also evaluated through the physical layer simulations and in terms of BER.

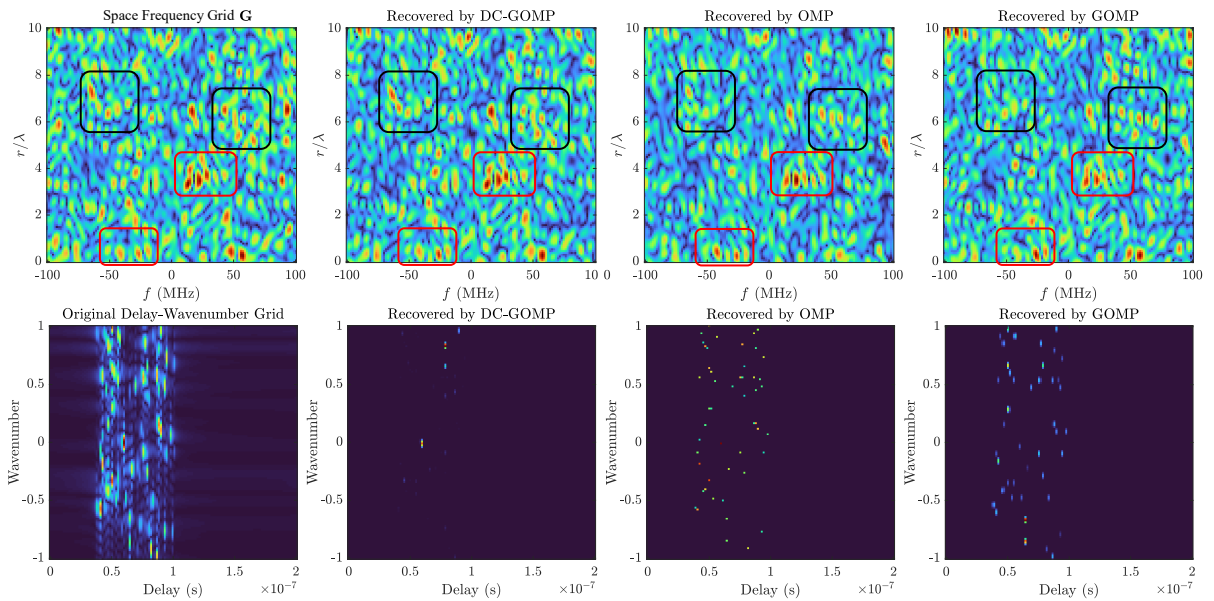


Figure 2. (1) The first row has four expressions in frequency-space domain. The first one represents the original SFG and the last three represent the recovered version by three different algorithm (our proposed DC-GOMP, OMP and GOMP). (2) Delay-wavenumber domain expressions corresponding to ones above. Black boxes denote the low power regions and red boxes denote the regions failing to correctly allocate the energy.

### A. Simulation Setup

In the simulations, we consider the FAS-assisted SIMO system where the receiver is equipped with the fluid array of different aperture sizes. We consider the maximal spread delay of the channel as  $2 \times 10^{-7}$  s, the signal bandwidth is 200 MHz, and the carrier frequency is 5.8 GHz. To obtain the SG of the doubly-selective frequency-space channel, the SFG with a  $128 \times 128$  grid is employed for the demand of sparsity. The effectiveness of the SE is evaluated by applying the antenna position optimization together with the MRC and frequency domain equalization at the receiver side.

### B. Results of Channel Estimation

We demonstrate the recovery performance of the SFG and its corresponding delay-wavenumber domain in Fig. 2 by using OMP, GOMP, and the proposed DC-GOMP scheme. Here, we consider  $M = K = 128$ ,  $N_r = 20$ ,  $N_p = 40$ ,  $L = 40$ , where the SNR is set to 10 dB and the aperture size is 10 times of the wavelength. Since the actual number of paths is not known at the receiver, we consider 50 iterations for all the algorithms and plot the performance corresponding to the best results for each algorithm. Obviously, our proposed DC-GOMP outperforms the other two in the details of the low power region (i.e., black boxes). The energy allocation within the red box of OMP and GOMP mismatches, but DC-GOMP does not. The relative error is computed by

$$\text{Relative Error} = \|\hat{\mathbf{G}}/\|\hat{\mathbf{G}}\|_F - \mathbf{G}/\|\mathbf{G}\|_F\|_F, \quad (39)$$

where the three algorithms (DC-GOMP, OMP, GOMP) respectively have relative errors of 0.3768, 0.58949 and 0.51650. Additionally, the initial antennas' positions and the pilots' positions do have some impact on the performance of the recovery. In our simulations, the channel parameters are generated according to the uniformly stochastic distributions described in (3), which leads to better recovery performance for uniformly distributed initial positions.

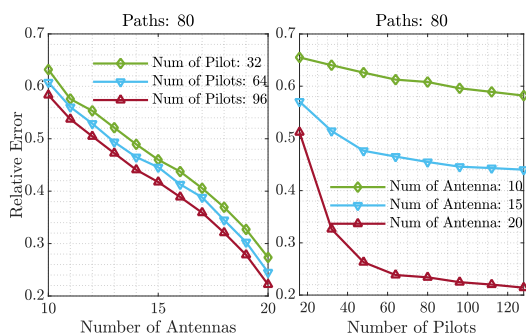


Figure 3. The performance trends of relative error of recovering SFG as the numbers of pilots and antennas varying.

In Fig. 3, we evaluate the performance scaling law with respect to the number of antennas and pilots. We consider an aperture size of  $10\lambda$  and SNR of 10 dB, where the number of paths is 80. Due to the assumption of one time slot the number of antennas denotes the samples in the space domain and the number of pilots in the frequency domain. Obviously, the number of spatial samples affects the relative error of the recovery more than the number of pilots. According to Nyquist's sampling theorem, spatial feature

recovery for an aperture of  $10\lambda$  requires at least 20 spatial sampling points. Nonetheless, given the prior knowledge of the physical modeling of propagation and the assumption of group sparsity, a sample of fewer than 20 antennas is sufficient for effective channel recovery. Generally, most SFG details can be successfully recovered when the relative error is less than 0.5, e.g., the relative error of recovered SFG in the first row and second column of Fig. 2 is 0.3768. As demonstrated in the right side of the graph above, with 20 antennas, the gain from increasing the number of guides decreases significantly beyond 40 in one-time slot recovery. By maintaining a constant channel over several time slots, multiple observations allow for a significant reduction in terms of the pilot overhead.

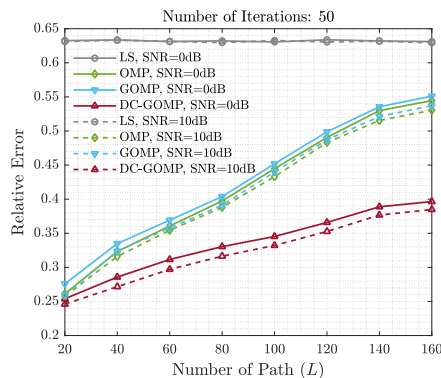


Figure 4. Comparison of four different algorithms on the performance of SFG recovering versus the number of paths.

Fig. 4 and Fig. 5 respectively show the superiority of our proposed DC-GOMP on the performance and the convergence rate compared to the classical OMP and GOMP. All the results in Fig. 4 are evaluated under the 50 iterations. As the number of paths rises, DC-GOMP significantly outperforms OMP and GOMP, while traditional methods like least square (LS) fail to work due to the fact that they cannot exploit the sparsity. For environments with large numbers of paths, the leakage effects of these paths hinder accurate recovery in the sparse domain as analyzed in Section IV-A, which significantly degrades the capability of traditional sparse recovery methods. Fig. 5 shows the convergence performances of DC-GOMP, OMP and GOMP. For each iteration of all three matching pursuit-like algorithms, the primary computational demands are associated with the LS and residual projection, i.e., step 8 and step 4 in algorithm 1. That means the time complexity of DC-GOMP is much less than that of the other two.

### C. Results of Spatial Equalization

Fig. 7 demonstrates the role of the FAS when performing SE under different aperture sizes ( $2\lambda$ ,  $6\lambda$ , and  $10\lambda$ ), corresponding to different numbers of antennas. The term 'Equal' refers to the maximum ratio combined channel response of the fixed equal-spaced array, and the term 'SE' refers to that of the spatially equalized FAS. Due to the global optimality guarantee, the result of SE in Fig. 7 is obtained by solving the MILP by the branch-and-bound method. The distinct coverage regions, represented by the blue and orange shaded areas, visually demonstrate the effectiveness of SE.

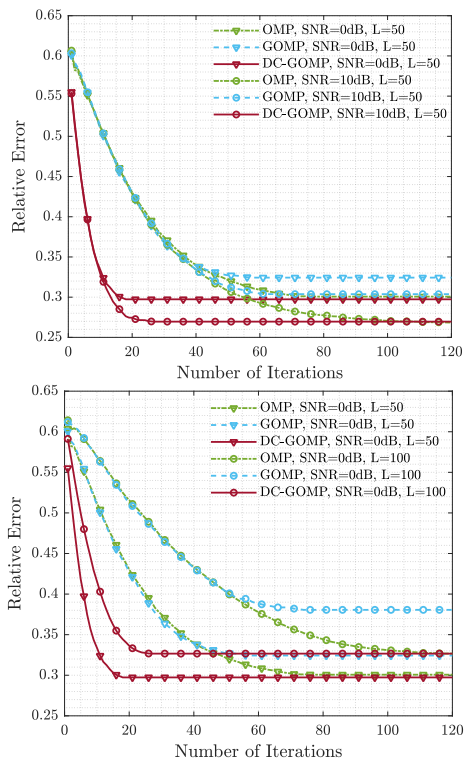


Figure 5. Convergence rate of three algorithms for different SNRs and numbers of paths.

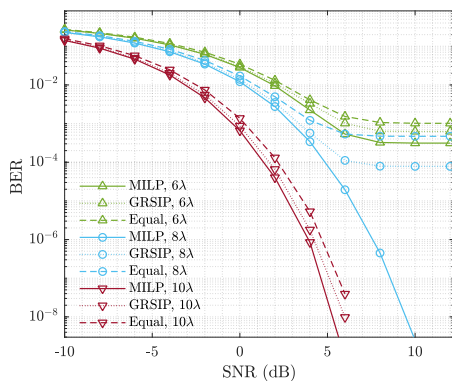


Figure 6. Comparison of the BER for different aperture size configurations under three position arrangement strategy versus SNR.

Notably, the worst gain of the subcarrier of the blue region exhibits an improvement of 10~15 dB compared to the orange region, confirming SE's capability to significantly reduce the probability of deep fading events. We find that SE's effectiveness increases with larger aperture sizes. The SE not only reduces deep fading but also boosts the average SNR of the combined channel by around 2 dB in the case of  $10\lambda$ , as indicated by 'average' in Fig. 7. This average SNR improvement scales with aperture size.

Fig. 6 demonstrates the BER performance for different position arrangements, including equal-spaced, MILP, and GRSIP. The simulation setup includes aperture sizes of  $6\lambda$ ,  $8\lambda$ , and  $10\lambda$ , corresponding to 12, 16, and 20 antennas, respectively. Under the QPSK constellation, we observe that the other two SE algorithms outperform the equal-spaced arrangement in terms of BER, especially with high SNR. We compare the  $6\lambda$  aperture and 12 antennas FAS-assisted

receiver applying SE to the 'Equal', where the 'MILP' eliminates the error floor up to a BER of  $10^{-8}$ , and the 'GRSIP' lowers the error floor below a BER of  $10^{-4}$ . It is observed that "MILP,  $6\lambda$ " outperforms "Equal,  $8\lambda$ ", indicating that SE can achieve comparable performance with fewer antennas or smaller aperture sizes.

## VI. CONCLUSION

This work established a unified framework for channel estimation and spatial equalization in FAS. We proposed a group-sparse recovery method with theoretical guarantees to address sparsity degradation under practical aperture constraints. A dynamic correlation-aware algorithm (DC-GOMP) was developed to overcome coherence limitations in sparse reconstruction, demonstrating significant improvements over conventional compressive sensing methods. Furthermore, the spatial equalization formulation (i.e., MILP) bridged combinatorial configurations of antennas' positions with continuous channel characteristics, enabling FAS to achieve performance comparable to larger fixed arrays. The framework establishes a foundational connection between wireless propagation and computational signal processing, advancing FAS implementations for 6G communications. Future work will extend this approach to dynamic multi-user environments and learning-based channel adaptation.

## APPENDIX A PROOF OF THEOREM 1

### A. Preliminary

Rewrite the noisy observation model as  $\mathbf{y}_0 = \mathbf{S}\mathbf{g}_0 + \mathbf{z} = \mathbf{S}\mathbf{D}\mathbf{x}_0 + \mathbf{z}$  and the modified convex second order cone program

$$\begin{aligned} \hat{\mathbf{g}} &= \arg \min_{\mathbf{g}} \|\mathbf{D}^H \mathbf{g}\|_{2,\mathcal{J}} \\ &\text{s.t. } \|\mathbf{S}\mathbf{g} - \mathbf{y}_0\|_2 \leq \varepsilon. \end{aligned} \quad (40)$$

Denoting the  $(\mathbf{D}^H \mathbf{g})^{(k)}$  as the vector consisting of the largest  $k$  groups in  $\mathbf{D}^H \mathbf{g}$ . Assuming  $\mathbf{x}_0$  is a group  $k$ -sparse vector and  $\mathbf{S}\mathbf{D}$  satisfies the group RIP with restricted isometry constants  $\delta_k < \sqrt{2} - 1$ , the group RIP is defined in [32].

Denoting by  $\mathbf{D}_T$  the matrix  $\mathbf{D}$  restricted to the column-groups indexed by  $T$ , which means that  $\mathbf{D}_T$  is the same as  $\mathbf{D}$  only at the columns with indices  $i \in T$  where  $T$  is the union of certain column-groups. Let  $T_0$  denote the set of the largest  $k$  group of  $\mathbf{D}^H \mathbf{g}$  in  $\ell_{2,\mathcal{J}}$ -norm. Divide the groups' indices  $T_0^c$  into a set of size  $M$  in order to decrease  $\ell_{2,\mathcal{J}}$ -norm of  $\mathbf{D}^H \mathbf{h}$  where  $\mathbf{h} = \mathbf{g}_0 - \hat{\mathbf{g}}$ , i.e.,  $\|\mathbf{D}_{T_1}^H \mathbf{h}\|_{2,\mathcal{J}} \geq \|\mathbf{D}_{T_2}^H \mathbf{h}\|_{2,\mathcal{J}} \geq \dots$ .  $P$  is usually taken as an integer multiple of  $k$ , and  $P > k$ .

Two common inequalities are given here, for any values  $u, v$  and  $c > 0$ ,

$$uv \leq \frac{cu^2}{2} + \frac{v^2}{2c}, \quad \sqrt{u^2 + v^2} \leq u + v. \quad (41)$$

### B. Bounding the Tail

The tail of recovery can be expressed as  $\sum_{i \geq 2} \|\mathbf{D}_{T_i}^H \mathbf{h}\|_2$ . Since the  $\hat{\mathbf{y}}$  is the global optimum of problem (40) so that

$$\begin{aligned} &\|\mathbf{D}^H \mathbf{g}_0\|_{2,\mathcal{J}} \\ &= \|\mathbf{D}_{T_0}^H \mathbf{g}_0\|_{2,\mathcal{J}} + \|\mathbf{D}_{T_0^c}^H \mathbf{g}_0\|_{2,\mathcal{J}} \\ &\geq \|\mathbf{D}_{T_0}^H (\mathbf{g}_0 - \mathbf{h})\|_{2,\mathcal{J}} + \|\mathbf{D}_{T_0^c}^H (\mathbf{g}_0 - \mathbf{h})\|_{2,\mathcal{J}} \\ &\geq \|\mathbf{D}_{T_0}^H \mathbf{g}_0\|_{2,\mathcal{J}} - \|\mathbf{D}_{T_0}^H \mathbf{h}\|_{2,\mathcal{J}} + \|\mathbf{D}_{T_0^c}^H \mathbf{h}\|_{2,\mathcal{J}} - \|\mathbf{D}_{T_0^c}^H \mathbf{g}_0\|_{2,\mathcal{J}}, \end{aligned}$$

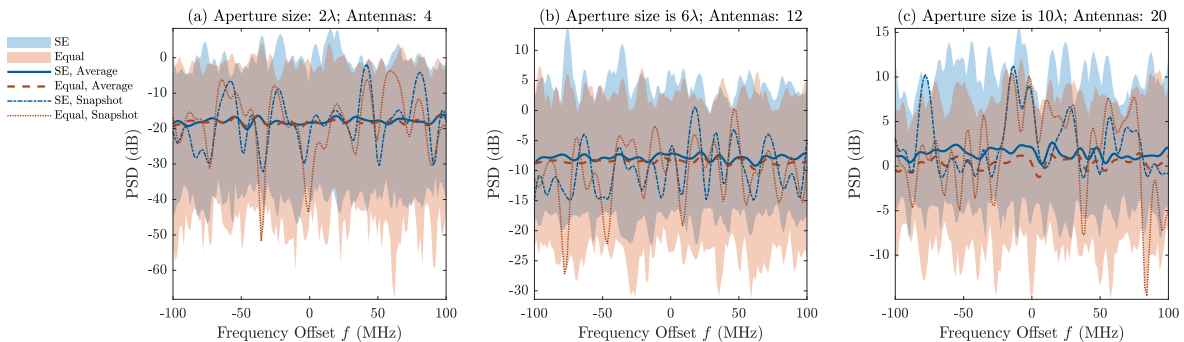


Figure 7. The combined PSDs demonstrate the application of SE by FAS versus no SE by a fixed equally spaced array for different aperture sizes. The colored shadows and bolder lines respectively denote the range and the average of combined PSDs of 100 times trials. The thinner line denotes one snapshot of two configurations.

which leads to the cone constraint

$$\|\mathbf{D}_{T_0}^H \mathbf{h}\|_{2,\mathcal{J}} \leq 2\|\mathbf{D}_{T_0}^H \mathbf{g}_0\|_{2,\mathcal{J}} + \|\mathbf{D}_{T_0}^H \mathbf{h}\|_{2,\mathcal{J}} \quad (42)$$

For simplicity of notation set  $T_{01} = T_0 \cup T_1$ ,  $\rho = k/P$  and the tail as  $\eta = 2\|\mathbf{D}_{T_0}^H \mathbf{g}_0\|_{2,\mathcal{J}}$ . We have

$$P^{\frac{1}{2}} \sum_{i \geq 2} \|\mathbf{D}_{T_i}^H \mathbf{h}\|_2 \leq \sum_{i \geq 1} \|\mathbf{D}_{T_i}^H \mathbf{h}\|_{2,\mathcal{J}} = \|\mathbf{D}_{T_0}^H \mathbf{h}\|_{2,\mathcal{J}} \quad (43)$$

and Cauchy-Schwarz leads to

$$\|\mathbf{D}_{T_0}^H \mathbf{h}\|_{2,\mathcal{J}} \leq k^{\frac{1}{2}} \|\mathbf{D}_{T_0}^H \mathbf{h}\|_2. \quad (44)$$

Then along with cone constraint in (42) we have

$$\sum_{i \geq 2} \|\mathbf{D}_{T_i}^H \mathbf{h}\|_2 \leq \sqrt{\rho} (\|\mathbf{D}_{T_0}^H \mathbf{h}\|_2 + \eta) \quad (45)$$

### C. Consequence of D-GRIP

The observation error vector  $\mathbf{S}\mathbf{h}$  satisfies the following

$$\begin{aligned} \|\mathbf{S}\mathbf{h}\|_2 &= \|\mathbf{S}\mathbf{g}_0 - \mathbf{S}\hat{\mathbf{g}}\|_2 \\ &\leq \|\mathbf{S}\mathbf{g}_0 - \mathbf{y}_0\|_2 + \|\mathbf{S}\hat{\mathbf{g}} - \mathbf{y}_0\|_2 \leq 2\varepsilon. \end{aligned} \quad (46)$$

Since  $\mathbf{D}$  is a tight frame and normalized by  $\mathbf{D}\mathbf{D}^H$ , along with D-GRIP and (45), we have

$$\begin{aligned} \|\mathbf{S}\mathbf{h}\|_2 &= \|\mathbf{S}\mathbf{D}\mathbf{D}^H \mathbf{h}\|_2 \\ &\geq \|\mathbf{S}\mathbf{D}_{T_{01}} \mathbf{D}_{T_{01}}^H \mathbf{h}\|_2 - \sum_{i \geq 2} \|\mathbf{S}\mathbf{D}_{T_i} \mathbf{D}_{T_i}^H \mathbf{h}\|_2 \\ &\stackrel{\text{D-GRIP}}{\geq} \sqrt{1 - \delta_{k+P}} \|\mathbf{D}_{T_{01}}^H \mathbf{h}\|_2 - \sqrt{1 + \delta_P} \sum_{i \geq 2} \|\mathbf{D}_{T_i}^H \mathbf{h}\|_2 \\ &\stackrel{(45)}{\geq} \sqrt{1 - \delta_{k+P}} \|\mathbf{D}_{T_{01}}^H \mathbf{h}\|_2 - \sqrt{\rho(1 + \delta_P)} (\|\mathbf{D}_{T_0}^H \mathbf{h}\|_2 + \eta) \\ &\stackrel{(45)}{\geq} \sqrt{1 - \delta_{k+P}} \|\mathbf{D}_{T_{01}}^H \mathbf{h}\|_2 - \sqrt{\rho(1 + \delta_P)} (\|\mathbf{h}\|_2 + \eta) \end{aligned} \quad (47)$$

Combining (46) and (47), we have

$$\sqrt{1 - \delta_{k+P}} \|\mathbf{D}_{T_{01}}^H \mathbf{h}\|_2 - \sqrt{\rho(1 + \delta_P)} (\|\mathbf{h}\|_2 + \eta) \leq 2\varepsilon \quad (48)$$

### D. Bounding the Error

The error vector  $\mathbf{h}$  has the norm that satisfies

$$\begin{aligned} \|\mathbf{h}\|_2^2 &= \|\mathbf{D}^H \mathbf{h}\|_2^2 \\ &\leq \|\mathbf{D}_{T_{01}}^H \mathbf{h}\|_2^2 + \|\mathbf{D}_{T_{01}^c}^H \mathbf{h}\|_2^2 \\ &\stackrel{(45)}{\leq} \|\mathbf{D}_{T_{01}}^H \mathbf{h}\|_2^2 + \rho (\|\mathbf{h}\|_2 + \eta)^2 \\ &\leq \|\mathbf{D}_{T_{01}}^H \mathbf{h}\|_2^2 + \rho (\|\mathbf{h}\|_2^2 + 2\eta\|\mathbf{h}\|_2 + \eta^2) \\ &\stackrel{(41)}{\leq} \|\mathbf{D}_{T_{01}}^H \mathbf{h}\|_2^2 + \rho (\|\mathbf{h}\|_2^2 + c\|\mathbf{h}\|_2^2 + \eta^2/c + \eta^2) \\ &\stackrel{(41)}{\leq} \frac{1}{\sqrt{1 - \rho - \rho c}} \left( \|\mathbf{D}_{T_{01}}^H \mathbf{h}\|_2 + \eta\sqrt{\rho(1 + 1/c)} \right) \\ &\stackrel{(48)}{\leq} \frac{2\varepsilon + \sqrt{\rho(1 + \delta_P)} (\|\mathbf{h}\|_2 + \eta)}{\sqrt{1 - \delta_{k+P}} \sqrt{1 - \rho - \rho c}} + \frac{\eta\sqrt{\rho(1 + 1/c)}}{\sqrt{1 - \rho - \rho c}} \end{aligned} \quad (49)$$

Substituting  $\eta$  into (49), we have the conclusion

$$\|\mathbf{h}\|_2 \leq C_0 \|\mathbf{D}^H \mathbf{g}_0 - (\mathbf{D}^H \mathbf{g}_0)^{(k)}\|_{2,\mathcal{J}} + C_1 \varepsilon \quad (50)$$

where

$$C_0 = 2 \frac{a\sqrt{1 - \delta_{k+P}} + \sqrt{1 + \delta_P}}{b\sqrt{1 - \delta_{k+P}} - \sqrt{1 + \delta_P}}, \quad (51)$$

$$C_1 = \frac{2}{b\sqrt{\rho}\sqrt{1 - \delta_{k+P}} - \sqrt{1 + \delta_P}}, \quad (52)$$

and  $c$  is any positive value,  $a = \sqrt{1 + \frac{1}{c}}$ ,  $b = \sqrt{\frac{1}{\rho} - 1 - c}$ .  $\blacksquare$

## APPENDIX B

### PROOF OF LEMMA 1 AND THEOREM 2

The ellipse-like support  $(\theta, \tau)$  of the leakage satisfies that

$$\left( \frac{8c}{WB(2\omega_c - B) |\cos \theta_l - \cos \theta| |\tau_l - \tau|} \right)^2 \geq T, \quad (53)$$

which can be relaxed into rectangle-like region as

$$\left( \frac{4c}{W(2\omega_c - B) |\cos \theta_l - \cos \theta|} \right)^2 \geq T, \quad (54)$$

$$\left( \frac{2}{B |\tau_l - \tau|} \right)^2 \geq T. \quad (55)$$

In order to guarantee the size of leakage support at different angle, we transform the angular domain into the wavenumber domain, i.e.,  $\mathbf{k}_\theta = \cos \theta$ , so that (54) becomes

$$\left( \frac{4c}{W(2\omega_c - B) |\mathbf{k}_{\theta_l} - \mathbf{k}_\theta|} \right)^2 \geq T. \quad (56)$$

By simple arithmetic, we have

$$\frac{2}{B\sqrt{T}} \geq |\tau_l - \tau|, \quad \frac{4c}{W\sqrt{T}(2\omega_c - B)} \geq |\mathbf{k}_{\theta_l} - \mathbf{k}_{\theta}|. \quad (57)$$

so that given the resolutions in delay domain and wavenumber domain, Lemma 1 can be obtained.

Using the identities  $\frac{B}{\Delta\omega} = \frac{\tau_{\max}}{\Delta\tau} = K$ ,  $\frac{2}{\Delta\mathbf{k}_{\theta}} = \frac{W}{\Delta r} = M$ , and (57), Theorem 2 can be obtained. ■

## REFERENCES

- [1] I. T. U. (ITU), “Framework and overall objectives of the future development of int for 2030 and beyond,” *ITU-R Recommendation M.2160*, 2023.
- [2] K.-K. Wong, K.-F. Tong, Y. Shen, Y. Chen, and Y. Zhang, “Bruce lee-inspired fluid antenna system: Six research topics and the potentials for 6g,” *Front. Commun. Networks*, vol. 3, p. 853416, 2022.
- [3] K.-K. Wong, A. Shojaefard, K.-F. Tong, and Y. Zhang, “Fluid antenna systems,” *IEEE Trans. Wireless Commun.*, vol. 20, no. 3, pp. 1950–1962, 2020.
- [4] K.-K. Wong and K.-F. Tong, “Fluid antenna multiple access,” *IEEE Trans. Wireless Commun.*, vol. 21, no. 7, pp. 4801–4815, 2021.
- [5] K.-K. Wong, D. Morales-Jimenez, K.-F. Tong, and C.-B. Chae, “Slow fluid antenna multiple access,” *IEEE Trans. Commun.*, vol. 71, no. 5, pp. 2831–2846, 2023.
- [6] W. K. New, K.-K. Wong, H. Xu, K.-F. Tong, and C.-B. Chae, “Fluid antenna system: New insights on outage probability and diversity gain,” *IEEE Trans. Wireless Commun.*, vol. 23, no. 1, pp. 128–140, 2023.
- [7] —, “An information-theoretic characterization of mimo-fas: Optimization, diversity-multiplexing tradeoff and q-outage capacity,” *IEEE Trans. Wireless Commun.*, vol. 23, no. 6, pp. 5541–5556, 2023.
- [8] H. Xu, K.-K. Wong, W. K. New, F. R. Ghadi, G. Zhou, and R. Murch, “Capacity maximization for fas-assisted multiple access channels,” *IEEE Trans. Commun.*, 2024.
- [9] K. K. Wong, A. Shojaefard, K.-F. Tong, and Y. Zhang, “Performance limits of fluid antenna systems,” *IEEE Commun. Lett.*, vol. 24, no. 11, pp. 2469–2472, 2020.
- [10] J. Yao, J. Zheng, T. Wu, M. Jin, C. Yuen, K.-K. Wong, and F. Adachi, “Fas-ris communication: Model, analysis, and optimization,” *IEEE Trans. Veh. Technol.*, 2025.
- [11] X. Lai, J. Yao, K. Zhi, T. Wu, D. Morales-Jimenez, and K.-K. Wong, “Fas-ris: A block-correlation model analysis,” *IEEE Trans. Veh. Technol.*, 2024.
- [12] C. Wang, G. Li, H. Zhang, K.-K. Wong, Z. Li, D. W. K. Ng, and C.-B. Chae, “Fluid antenna system liberating multiuser mimo for isac via deep reinforcement learning,” *IEEE Trans. Wireless Commun.*, 2024.
- [13] T. Hao, C. Shi, Q. Wu, B. Xia, Y. Guo, L. Ding, and F. Yang, “Fluid-antenna enhanced isac: Joint antenna positioning and dual-functional beamforming design under perfect and imperfect csi,” *arXiv preprint arXiv:2407.18988*, 2024.
- [14] L. Zhang, H. Yang, Y. Zhao, and J. Hu, “Joint port selection and beamforming design for fluid antenna assisted integrated data and energy transfer,” *IEEE Wireless Commun. Lett.*, 2024.
- [15] X. Dong, X. Ren, B. Lai, R. Xiong, T. Mi, and R. C. Qiu, “Wireless communications in cavity: A reconfigurable boundary modulation based approach,” in *ICC 2024-IEEE International Conference on Communications*. IEEE, 2024, pp. 5553–5558.
- [16] L. Zhu, W. Ma, B. Ning, and R. Zhang, “Movable-antenna enhanced multiuser communication via antenna position optimization,” *IEEE Trans. Wireless Commun.*, vol. 23, no. 7, pp. 7214–7229, 2024.
- [17] W. Mei, X. Wei, B. Ning, Z. Chen, and R. Zhang, “Movable-antenna position optimization: A graph-based approach,” *IEEE Wireless Commun. Lett.*, vol. 13, no. 7, pp. 1853–1857, 2024.
- [18] X. Wei, W. Mei, D. Wang, B. Ning, and Z. Chen, “Joint beamforming and antenna position optimization for movable antenna-assisted spectrum sharing,” *IEEE Wireless Commun. Lett.*, vol. 13, no. 9, pp. 2502–2506, 2024.
- [19] W. K. New, K.-K. Wong, H. Xu, F. R. Ghadi, R. Murch, and C.-B. Chae, “Channel estimation and reconstruction in fluid antenna system: Oversampling is essential,” *IEEE Trans. Wireless Commun.*, 2024.
- [20] Z. Zhang, J. Zhu, L. Dai, and R. W. Heath, “Successive bayesian reconstructor for channel estimation in fluid antenna systems,” *IEEE Trans. Wireless Commun.*, 2024.
- [21] C. Skouroumounis and I. Krikidis, “Fluid antenna with linear mmse channel estimation for large-scale cellular networks,” *IEEE Trans. Commun.*, vol. 71, no. 2, pp. 1112–1125, 2022.
- [22] H. Xu, G. Zhou, K.-K. Wong, W. K. New, C. Wang, C.-B. Chae, R. Murch, S. Jin, and Y. Zhang, “Channel estimation for fas-assisted multiuser mmwave systems,” *IEEE Commun. Lett.*, vol. 28, no. 3, pp. 632–636, 2023.
- [23] W. Ma, L. Zhu, and R. Zhang, “Compressed sensing based channel estimation for movable antenna communications,” *IEEE Commun. Lett.*, vol. 27, no. 10, pp. 2747–2751, 2023.
- [24] Z. Xiao, S. Cao, L. Zhu, Y. Liu, B. Ning, X.-G. Xia, and R. Zhang, “Channel estimation for movable antenna communication systems: A framework based on compressed sensing,” *IEEE Trans. Wireless Commun.*, 2024.
- [25] S. Ji, C. Psomas, and J. Thompson, “Correlation-based machine learning techniques for channel estimation with fluid antennas,” in *2024 IEEE International Conference on Acoustics, Speech and Signal Processing (ICASSP)*. IEEE, 2024, pp. 8891–8895.
- [26] R. Zhang, L. Cheng, W. Zhang, X. Guan, Y. Cai, W. Wu, and R. Zhang, “Channel estimation for movable-antenna mimo systems via tensor decomposition,” *IEEE Wireless Commun. Lett.*, 2024.
- [27] R. C. Qiu and I.-T. Lu, “Multipath resolving with frequency dependence for wide-band wireless channel modeling,” *IEEE Trans. Veh. Technol.*, vol. 48, no. 1, pp. 273–285, 1999.
- [28] R. C. Qiu, “A study of the ultra-wideband wireless propagation channel and optimum uwb receiver design,” *IEEE J. Sel. Areas Commun.*, vol. 20, no. 9, pp. 1628–1637, 2002.
- [29] G. Taubock, F. Hlawatsch, D. Eiwien, and H. Rauhut, “Compressive estimation of doubly selective channels in multicarrier systems: Leakage effects and sparsity-enhancing processing,” *IEEE J. Sel. Top. Signal Process.*, vol. 4, no. 2, pp. 255–271, 2010.
- [30] E. J. Candes, J. K. Romberg, and T. Tao, “Stable signal recovery from incomplete and inaccurate measurements,” *Commun. Pure Appl. Math.*, vol. 59, no. 8, pp. 1207–1223, 2006.
- [31] E. J. Candes, Y. C. Eldar, D. Needell, and P. Randall, “Compressed sensing with coherent and redundant dictionaries,” *Appl. Comput. Harmon. Anal.*, vol. 31, no. 1, pp. 59–73, 2011.
- [32] Y. C. Eldar and M. Mishali, “Robust recovery of signals from a structured union of subspaces,” *IEEE Trans. Inf. Theory*, vol. 55, no. 11, pp. 5302–5316, 2009.
- [33] E. J. Candès, J. Romberg, and T. Tao, “Robust uncertainty principles: Exact signal reconstruction from highly incomplete frequency information,” *IEEE Trans. Inf. Theory*, vol. 52, no. 2, pp. 489–509, 2006.
- [34] J. A. Tropp, “Greed is good: Algorithmic results for sparse approximation,” *IEEE Trans. Inf. Theory*, vol. 50, no. 10, pp. 2231–2242, 2004.
- [35] D. L. Donoho, X. Huo *et al.*, “Uncertainty principles and ideal atomic decomposition,” *IEEE Trans. Inf. Theory*, vol. 47, no. 7, pp. 2845–2862, 2001.
- [36] M. Elad and A. M. Bruckstein, “A generalized uncertainty principle and sparse representation in pairs of bases,” *IEEE Trans. Inf. Theory*, vol. 48, no. 9, pp. 2558–2567, 2002.
- [37] Y. C. Eldar, P. Kuppinger, and H. Bolcskei, “Block-sparse signals: Uncertainty relations and efficient recovery,” *IEEE Trans. Signal Process.*, vol. 58, no. 6, pp. 3042–3054, 2010.
- [38] X. Wang and E. Aboutanios, “Sparse array design for multiple switched beams using iterative antenna selection method,” *Digital Signal Process.*, vol. 105, p. 102684, 2020.
- [39] Y. Gao, H. Vinck, and T. Kaiser, “Massive mimo antenna selection: Switching architectures, capacity bounds, and optimal antenna selection algorithms,” *IEEE Trans. Signal Process.*, vol. 66, no. 5, pp. 1346–1360, 2017.
- [40] M. O. Mendonça, P. S. Diniz, T. N. Ferreira, and L. Lovisolo, “Antenna selection in massive mimo based on greedy algorithms,” *IEEE Trans. Wireless Commun.*, vol. 19, no. 3, pp. 1868–1881, 2019.
- [41] W. Huang, Y. Huang, Y. Zeng, and L. Yang, “Wideband millimeter wave communication with lens antenna array: Joint beamforming and antenna selection with group sparse optimization,” *IEEE Trans. Wireless Commun.*, vol. 17, no. 10, pp. 6575–6589, 2018.
- [42] O. K. Rasheed, G. Surabhi, and A. Chockalingam, “Sparse delay-doppler channel estimation in rapidly time-varying channels for multiuser ofds on the uplink,” in *2020 IEEE 91st vehicular technology conference (VTC2020-Spring)*. IEEE, 2020, pp. 1–5.
- [43] Y. Han and J. Lee, “Two-stage compressed sensing for millimeter wave channel estimation,” in *2016 IEEE International Symposium on Information Theory (ISIT)*. IEEE, 2016, pp. 860–864.
- [44] R. Xiong, X. Dong, T. Mi, K. Wan, and R. C. Qiu, “Optimal discrete beamforming of ris-aided wireless communications: An inner product maximization approach,” in *2024 IEEE Wireless Communications and Networking Conference (WCNC)*. IEEE, 2024, pp. 1–6.